Dynamic-Stall-Driven Vertical Axis Wind Turbine: An Experimental Study

David Keisar*†[1], Idan Arava[2]† and David Greenblatt†[3]

** Massachusetts Institute of Technology, Cambridge, Massachusetts, USA*

†Technion – Israel Institute of Technology, Technion City, Haifa 3200003, Israel

Abstract

The driving torque on vertical axis wind turbines with large chord-to-radius ratio blades, typically greater than 0.5, is generated mainly by the phenomenon of dynamic stall. In order to determine the optimum configuration, an extensive experimental study was conducted on two-bladed, H-rotor test turbine, by systematically varying the blade chord-to-radius ratio, blade profile (NACA 0012 and NACA 0021), preset angle, strut-blade offset and Reynolds number. Unlike low solidity turbines, peak power coefficients were virtually independent of the chord-to-radius ratio in the range of 0.6 to 0.85 for both blade profiles. At low Reynolds numbers ($\sim 10^5$), turbine performance with NACA 0021 blades was vastly superior to that with NACA 0021 blades, producing approximately 90% greater power and torque coefficients at blade tip-speed to wind speed ratios between 0.8 and 1.6. The attainment of peak power and torque coefficients greater than 30% at low rotational speeds and Reynolds numbers renders these turbines highly applicable to urban and low wind speed applications. On the basis of blade-mounted phase-resolved tufts images, it was concluded that an aft dynamic stall vortex precedes the conventional leading-edge vortex on the NACA 0021, resulting in substantially greater post-stall dynamic lift. Preset angles away from zero degrees and variations in strut-blade offset away from the half-chord position reduced turbine performance, due to changes in the nature of dynamic stall. The similarity between preset and offset effects was explained by a new approach of a virtual preset angle that depends on the offset point.

---

[1] Corresponding author, Postdoctoral Associate, Massachusetts Institute of Technology, Faculty of Mechanical Engineering. keisar@mit.edu.

[2] M.Sc. Student, Technion – Israel Institute of Technology, Faculty of Mechanical Engineering.

[3] Professor, Technion – Israel Institute of Technology, Faculty of Mechanical Engineering. davidg@technion.ac.il.

1 Introduction

Off-grid and decentralized microgrid systems represent a steadily growing segment of the energy industry that can operate autonomously or semi-autonomously with large-scale power utilities [1,2]. The two key drivers are small-scale (<100kW) solar and wind energy technologies. Small wind turbines, in particular, have the potential to be a significant contributor to the energy mix, accumulating over 1 GW of installed capacity [3]. Although, in the past, large lift-based vertical axis wind turbines (VAWT) were considered unreliable due to structural integrity [4], research interest in small-scale VAWTs peaked in recent years due to their vast potential. Much of the research is centered on urban-scale implementation [5], arising from well-known advantages such as insensitivity to the wind direction [6] and the ground-level location of the generator or load.

Recently, we studied a new mechanism of lift-based wind power generation where the *phenomenon of dynamic stall* is responsible for driving VAWTs to maximum power, when the blade-chord, c, to turbine radius, R, is relatively large $\varepsilon \equiv c/R \gtrsim 0.5$ [7]. This approach dispenses with conventional fluid-machinery design philosophy, which consistently and uniformly seeks to avoid boundary layer separation. We refer to this as a <u>d</u>ynamic <u>s</u>tall-<u>d</u>riven wind <u>t</u>urbine (DSDT). The key to understanding and exploiting this DSDT relies on effectively managing the dynamic stall process, or the leading-edge dynamic stall vortex in the case of thin blades. The aim is to produce a beneficial lift-producing dynamic stall effect [8,9] on the blades when the relative dynamic pressure is high and allow detrimental shedding of the vortex when the dynamic pressure is low. Increases in solidity $\sigma \equiv Nc/R = N\varepsilon$ by increasing the number of blades, N, generally reduce peak turbine performance [10]. In contrast, increasing solidity by increasing ε, may increase the turbine's performance [7,11].

VAWTs with large ε also offer additional potential advantages. First, the larger blade chord lengths result in proportionally thicker blades with greater structural stiffness. Second, the chord-based Reynolds numbers are relatively high for a given turbine radius and rotational speed, which is highly advantageous at low wind speeds or small to medium scales [12,13]. Third, the high solidity produces high torque with superior self-starting abilities, ideal for high-pressure pumping [14]. Finally, the high turbine solidity with large, slow-moving blades poses a significantly lower danger to bird life [15] and noise emissions [16]. These factors are highly consequential for urban installations and in countries with significant bird migratory routes [17].

Given the advantages of the DSDT concept, this paper reports on an extensive experimental study that was undertaken with the objective of maximizing the turbine power and determining the limitations of the system. In particular, the effect of blade profile, turbine geometry, and wind speed on power, torque, and operational range was investigated. A dedicated H-rotor VAWT facility was constructed that allowed variation of chord-to-radius ratio, ε, strut-blade connection point (blade offset), x_c / c, blade preset pitch angle, β and blade profile. NACA 0012 and NACA 0021 blade profiles, characterizing prototypical leading-edge and trailing-edge stall mechanisms, were employed. All evaluations were conducted in a blower-type wind tunnel, where wind speed could be precisely controlled. The paper is structured as follows: section 2 briefly explains DSDT concepts; section 3 describes the experimental facility and data acquisition methods; section 4 presents the major findings of the study along with a discussion of these results; and section 5 summarizes the main conclusions.

2 Factors Affecting DSDT Performance

Although dynamic stall models have been used to predict low solidity $(\sigma < 0.4)$ turbine performance using blade-element momentum methods [18], there is no general method for predicting deep dynamic stall associated with DSDT performance. This is partly due to the large angle-of-attack range (well in excess of the static stall angle), the decisive effect of the strut-blade connection point [7], the large dimensionless pitch-rates, as well as angle-of-attack and dynamic pressure variations along the chord of the blade. The manner in which these factors affect DSDT performance is discussed in sections 2.1 to 2.4, below.

2.1 The Phenomenon of Dynamic Stall

The impact of deep dynamic stall on DSDTs performance can be understood by considering our fundamental experimental studies described in [18–22], briefly summarized in this section. Consider a thick symmetric airfoil (NACA 0018) undergoing large-amplitude, harmonic pitching according to $\alpha = 30° \sin(\omega t)$ at $Re_c \equiv cU_\infty / \nu = 2.5 \times 10^5$ where α is the airfoil angel-of-attack, $\omega \equiv 2\pi f$ is the airfoil pitching frequency, c is the airfoil chord, U_∞ is the freestream velocity and ν is the kinematic viscosity. We define the dimensionless pitch-rate as $k \equiv \omega c / 2U_\infty$. The phase-averaged aerodynamic coefficients as a function of the angle of attack α for quasi-steady $(k = 10^{-4})$ and dynamic conditions ($k = 0.036$ and $k = 0.074$) are shown in Figure 3. Corresponding phase-averaged particle image velocimetry (PIV) velocity vectors and dimensionless vorticity for $k = 0.074$ are shown in Figure 2. A dashed line and a dotted line indicate the pressure coefficient on the low and high surfaces, respectively.

Quasi-steady aerodynamic coefficients show gentle stall characteristics typical of a "trailing-edge stall," where separation gradually moves upstream with an increasing angle of attack (Figure 3). Also present is well-known "hysteresis" or bi-stable behavior, where the upstroke and downstroke do not separate and reattach symmetrically. During dynamic motion, the stall is delayed to higher angles-of-attack $\Delta\alpha_{\text{stall}}$ and higher maximum lift coefficients, $\Delta C_{l,\max}$, where larger k results in greater $\Delta\alpha_{\text{stall}}$ and $\Delta C_{l,\max}$. Corresponding pressure coefficient and PIV measurements at $\alpha = 20°$ show a leading-edge separation bubble and a thickening of the boundary layer over the aft part of the blade, with the associated reversed flow, which marks the onset of moment stall (Figure 2a). With increasing angle of attack ($\alpha = 24.5°$, Figure 2b), this aft region of reverse flow forms into what we termed an aft dynamic stall vortex (ADSV), while the leading-edge separation bubble continues to grow into what is commonly called a leading-edge vortex (LEV), or a dynamic stall vortex (DSV). These observations should be contrasted with common descriptions of a thin airfoil (typically $\leq 12\%$) dynamic stall [9,23], where there is no ADSV and the moment coefficient remains almost constant until the shedding of the (LEV). With increasing angle-of-attack, up to $\alpha = 26°$ (Figure 2c to Figure 2d), the continued growth of both vortices is responsible for further lift enhancement. However, they shed from the airfoil almost simultaneously, and ultimately merge, resulting in a precipitous loss of lift between $\alpha = 26.75°$ (Figure 2e) and $\alpha = 29°$ (Figure 2g). As the airfoil pitches down, the separated shear layer (e.g., at $\alpha = 20°$, Figure 2h), begins to reattach, initially at the leading-edge ($\alpha = 10°$, Figure 2i) and subsequently propagates to the trailing edge. At twice the Reynolds number, namely $Re_c = 5\times10^5$ (not shown here), the ADSV is weaker for a given k.

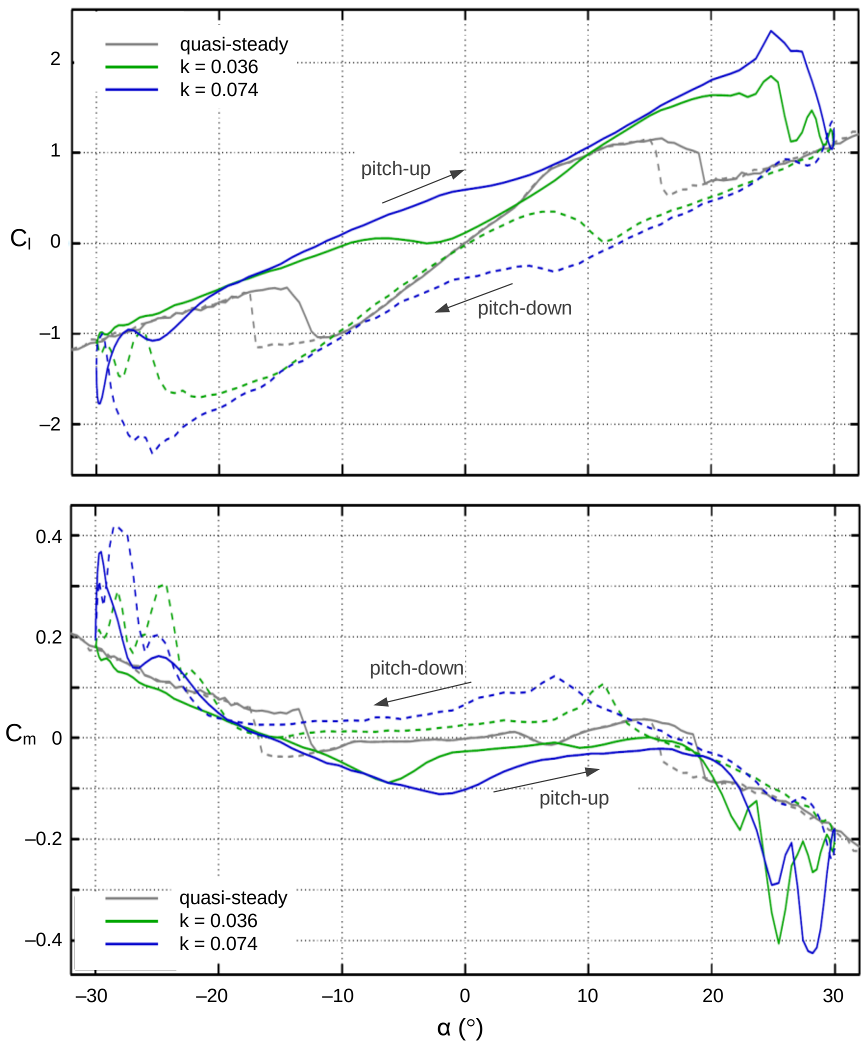

Figure 1: Phase-averaged lift and moment coefficients for a NACA 0018 pitching harmonically according to $\alpha = 30°\sin(\omega t)$ at $Re_c = 2.5\times10^5$, for various values of k.

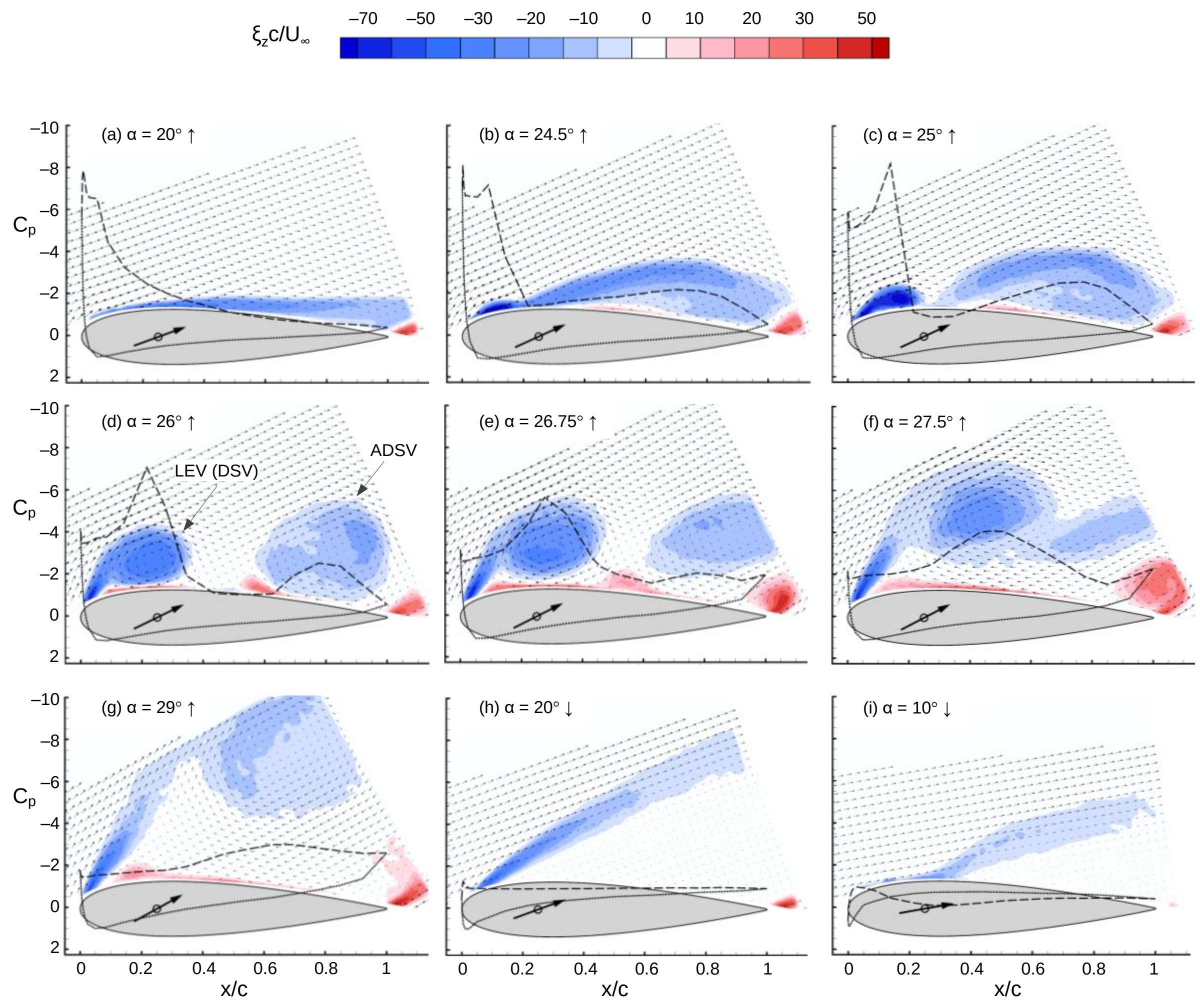

Figure 2: Phase-averaged velocity vectors (black arrows), vorticity fields (clockwise – blue; counter-clockwise – red), and surface pressure coefficients (low-pressure side – dashed line; high-pressure side – dotted line) of a NACA 0018 pitching harmonically at $\alpha = 30°\sin(\omega t)$, $Re_c = 2.5\times10^5$, and $k = 0.074$ (corresponding to Figure 1). Pitch-up (a-g) and pitch-down (h,i); arrows indicate pitch-up and pitch-down of the blade, respectively.

2.2 Simplified VAWT Blade Kinematics

The blades of a VAWT are subjected to cyclic variations in the relative wind velocity, W, with respect to the chord that affects the relative angle-of-attack α and the relative dynamic pressure $q \equiv \frac{1}{2}\rho|W|^2$, where ρ is the air density. Consider the top view cross-section of a turbine in a uniform freestream U_∞ shown in Figure 3, where θ is the blade's azimuthal angle, ω is the rotational speed, V_b is the blade's tangential velocity, and $\bar{U}_i$ is the induced velocity (assumed constant across the diameter). The coordinate x is measured from the blade leading-edge, R is the turbine radius, and x_c is the strut-blade connection point (or blade offset). From the figure, it can be seen that the blade's angle-of-attack at the strut-blade connection point x_c is:

$$\alpha = \tan^{-1}\left(\frac{\sin\theta}{\lambda' + \cos\theta}\right) + \beta \tag{1}$$

where $\lambda' = \lambda / (1 - \bar{a})$, $\bar{a} = 1 - \bar{U}_i / U_\infty$ is the average induction factor, β is the blade preset pitch angle, and:

$$\lambda \equiv \frac{\omega R}{U_\infty} \tag{2}$$

is the blade-freestream-velocity tip speed ratio (or simply tip speed ratio, TSR). Similarly, from Figure 3, the magnitude of the relative dynamic pressure at x_c is:

$$q_{\mathrm{rel}} \equiv \tfrac{1}{2}\rho |W|^2 = \tfrac{1}{2}\rho U_\infty^2 [(\lambda' + \cos\theta)^2 + \sin^2\theta] \tag{3}$$

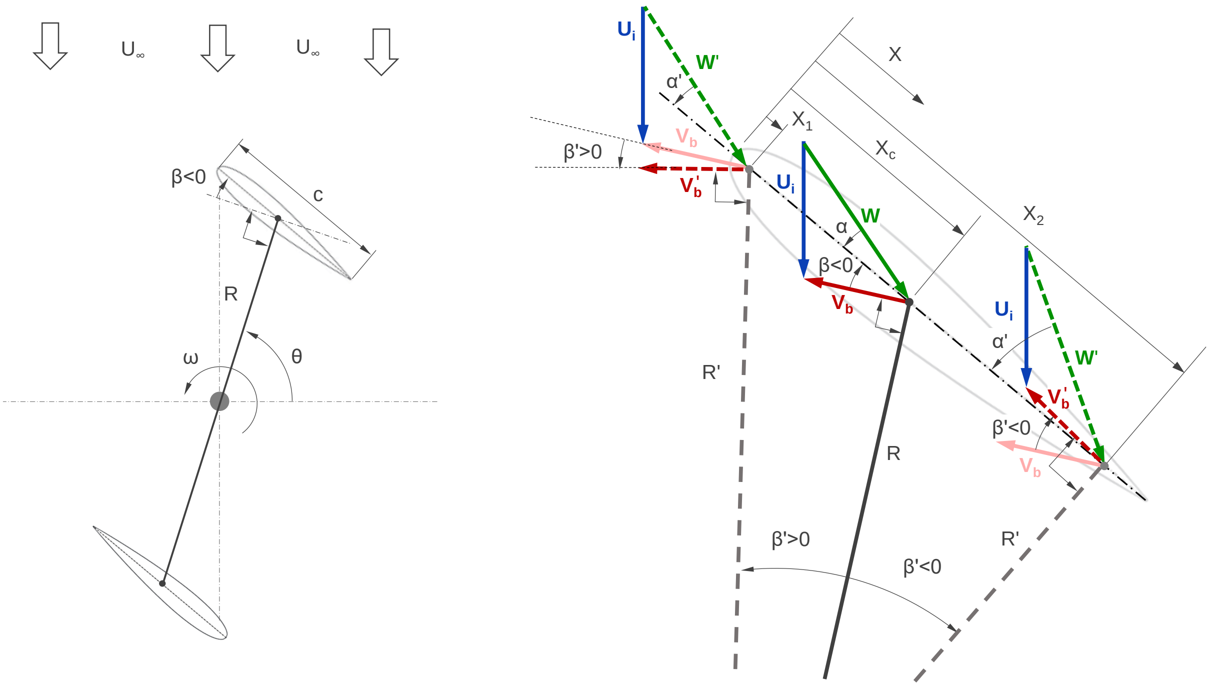

Figure 3: Schematic illustration defining the turbine geometry with a negative (pitch-down) preset pitch angle $\beta < 0$ (left); and the relevant velocity vectors at the strut-blade connection point, x_c , as well as upstream $(x = x_1)$ and downstream $(x = x_2)$ of x_c (right).

However, Figure 3 illustrates that the blades of VAWT with $\varepsilon >> 0$ experience significant variations in the local angle-of-attack α' and local dynamic pressure q'_{rel} along the blade chord (At $x = x_c$. $\alpha' = \alpha$ and $q'_{\text{rel}} = q_{\text{rel}}$) . The relevant velocity vectors upstream $(x = x_1)$ and downstream $(x = x_2)$ of the strut-blade connection point x_c are shown. Migliore et al. [24] suggested conformally transforming a symmetric blade profile and introduced the concept of "virtual camber" or "virtual angle-of-attack". Following the analysis in [7], the virtual angle-of-attack, or virtual camberline, along the blade chord can be expressed as:

$$\frac{dz'}{dx} = \alpha' - \alpha = \tan^{-1}\left(\frac{\sin(\theta + \beta')}{\lambda' + \cos(\theta + \beta')}\right) - \tan^{-1}\left(\frac{\sin\theta}{\lambda' + \cos\theta}\right) - \beta' \tag{4}$$

with:

$$\beta' = \tan^{-1}\left(\frac{x_c - x}{c}\varepsilon\right) \tag{5}$$

where the expression $-\beta' - \beta$ can be thought of as the "zero-wind $[U_\infty = 0]$ angle-of-attack" [25]. The virtual camber-line can be obtained by integrating eqn. (4) for various values of θ, λ', x_c and ε . Similarly, it can be shown that, upwind, the relative dynamic pressure, namely:

$$q'_{\text{rel}} = \tfrac{1}{2}\rho U_\infty^2 \{[\lambda' + \cos(\theta + \beta')]^2 + \sin^2(\theta + \beta')\} \tag{6}$$

increases along the chord. The virtual camber-line, at high ε turbines can reach high maximum cambering. For example, for a $\varepsilon = 0.6$ turbine, operating at $\lambda' = 1.5$, a symmetrical blade experiences a substetial parabolic cambering with a maximum camber of $z / c = 5\%$.

2.3 Blade Offset and Preset Pitch Angle

Fiedler and Tullis [25] determined that for symmetrical blades, peak turbine performance, at $\beta = 0$, was achieved when the blade was connected mid-chord, i.e., blade offset was zero, $x_c / c = 1/2$. Furthermore, they observed that performance losses obtained for a strut-blade connection closer to the leading-edge, $x_c / c < 1/2$, could be ameliorated by negative (pitch-down) preset angles $\beta < 0$. The reasoning behind this is that when $x_c / c < 1/2$, the virtual camberline undergoes a virtual pitch-up rotation around the connection point. This is comparable to a positive (pitch-up) preset pitch $\beta > 0$ and is thus compensated for by a negative preset pitch. They described their experimental findings on the basis of the "zero-wind angle-of-attack", $\alpha_0 = -\beta' - \beta$ defined in the previous section.

We can formally define the virtual preset angle from eqn. (4) as the difference between the camberline slope and its value at $x_c / c = 1/2$, namely:

$$\beta_{\text{vir}} = (dz'/dx)_{x_c/c=1/2} - dz'/dx = f(\lambda', x_c/c, x/c, \theta, \varepsilon) \tag{7}$$

This expression can be greatly simplified if we let $\lambda' = 1$, ignore the singularities at $\theta = 180°$ and $\theta + \beta' = 180°$, and assume small angles, which eliminates θ and x/c as parameters, to give:

$$\beta_{\text{vir}} \approx \frac{\varepsilon}{2}\left(\frac{1}{2} - \frac{x_c}{c}\right) \approx -\frac{\beta'}{2} \tag{8}$$

2.4 Dimensionless Pitch-Rate

In contrast to the low or intermediate solidity VAWTs, dynamic stall produces the vast majority of torque for rotation when ε is large and $\lambda \to 1$. This is because the lift overshoot at large angles-of-attack associated with pitch-up occurs when the relative dynamic pressure is high, producing substantial torque. Conversely, the shedding of the DSV occurs when the dynamic pressure is low, and thus its deleterious effects are reduced. Furthermore, the driving torque is only produced in the upwind quadrants, over the approximate range of azimuthal angles of $0° < \theta < 120°$, as shown in [10,11,26]. To illustrate this, consider the blade pitch-rate, $\dot{\alpha} \equiv d\alpha / dt$, at the strut-blade connection point, commonly expressed in the dimensionless form as:

$$\kappa \equiv \dot{\alpha} c / 2|W| \tag{9}$$

which controls the dynamic stall time-scales and lift overshoot [8,23,27–31]. Note that the pitch-rate, κ, and the harmonic oscillation, k, are different, where the former is commonly used to characterize transient angle-of-attack variations. Letting $\theta = \omega t$ and differentiating eqn. (1) with respect to time, results in the nominal blade pitch-rate at x_c / c, namely:

$$\dot{\alpha} \equiv \frac{d\alpha}{dt} = \frac{\omega(\lambda' \cos\theta + 1)}{\lambda^2 + 2\lambda' \cos\theta + 1} \tag{10}$$

Substituting eqns. (2), (10) and the absolute value of (3) into (9), we can show that:

$$\kappa = \frac{\varepsilon}{2} \frac{\lambda'(\lambda' \cos\theta + 1)}{(\lambda'^2 + 2\lambda' \cos\theta + 1)\sqrt{(\lambda' + \cos\theta)^2 + \sin^2\theta}} \tag{11}$$

Finally, for small values of θ, eqn. (11) reduces to the approximate *constant pitch-up* rate:

$$\kappa_{\text{up}} \approx \frac{\varepsilon}{2} \frac{\lambda'}{(\lambda'+1)^2} \tag{12}$$

which is linearly dependent on ε and weakly dependent on λ'. This is a significant result because it implies that data acquired on airfoils subjected to constant pitch-rate rotation [8] are directly relevant to DSDT aerodynamics.

Figure 4 (left) illustrates the idealized difference between the relative dynamic pressure, angle-of-attack, and pitch-rate for two turbines of identical solidity ($\sigma = 1.5$), namely: a DSDT ($N = 2$, $\varepsilon = 0.75$) and a conventional multibladed turbine $(N = 5,\ \varepsilon = 0.3)$. The blade static angle is assumed to be $\alpha_{\text{stall}} = 12°$, and the shaded area on the graphs represents post-static-stall angles-of-attack. We assume that peak power is attained at $\lambda = 1$ and that the induction factor $\bar{a} = \frac{1}{3}$ corresponds to the Betz limit, to yield $\lambda' = 1.5$. It is clear that the only difference is the value of the dimensionless pitch-rate κ , which increases by a factor of 2.5. This difference is critical for two reasons: first, increases in pitch rate bring about linear increases in peak lift coefficient, as described in section 2.1, that delay dynamic stall to higher angles-of-attack [8,32,33]; and second, the higher angles-of-attack at which dynamic stall occurs corresponds to lower dynamic pressures, as seen on the figure.

Figure 4 (right) is an illustration of the same parameters, corresponding to an intermediate solidity turbine (e.g., $\sigma = 0.6$, $\varepsilon = 0.2$ and $\lambda' = 3.5$) whose blades undergo light dynamic stall [34]. The differences between this type of configuration and the DSDT are substantial. Although the peak DSDT dynamic pressure is lower by a factor of >3, the dimensionless pitch-rate is higher by a factor of >5. Moreover, the DSDT dimensionless pitch-rate is almost constant, up to $\theta = 110°$, thereby delaying the shedding of the leading-edge vortex, where the dynamic pressure is significantly lower when compared to its peak value. In contrast, on medium solidity turbines, the pitch-rate decreases with pitch-up and goes negative when the angle-of-attach is at its maximum value. Shedding of the dynamic stall vortices typically occurs at these azimuthal angles during light stall, and the relatively high corresponding dynamic pressure, which is approximately ½ of its peak, exacerbates its adverse effects. Note, furthermore, that for an assumed static stall angle $\alpha_{\text{stall}} = 12°$, the stall azimuthal angle θ_{stall} changes, as can be seen by the post-stall fraction of the cycle (shaded area) that increases from 45% to 80%.

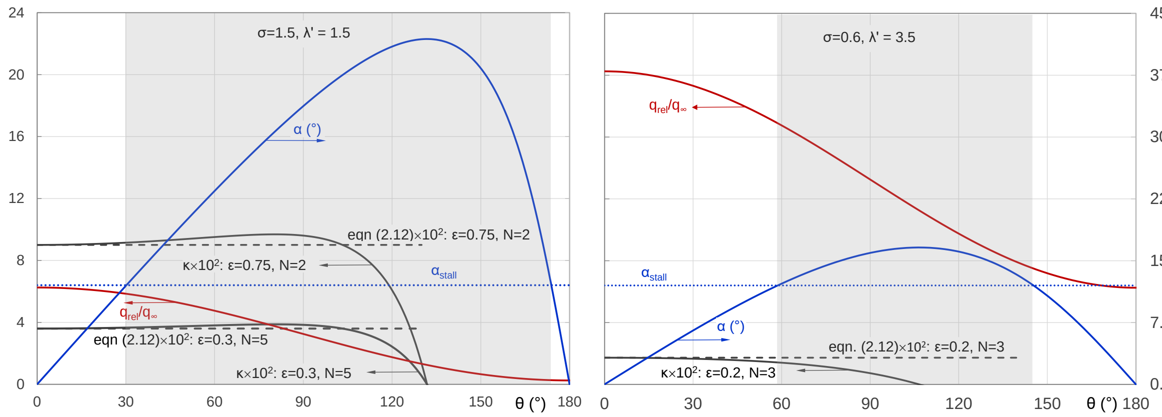

Figure 4: Variation of angle of attack, pitch-rate and relative dynamic pressure in the upwind quadrants for three idealized cases – left: $\sigma = 1.5$ and $\lambda' = 1.5$ ($\varepsilon = 0.75$, $N = 2$ and $\varepsilon = 0.3$, $N = 5$); right – $\sigma = 0.6$, $\varepsilon = 0.2$, $N = 3$ and $\lambda' = 3.5$. Static stall is assumed to occur at 12° where the shaded area on the curve represents post-stall angles-of-attack.

3 Experimental Setup

3.1 The Turbine Model

The H-rotor turbine employed in this study was designed with the express purpose of varying multiple parameters, namely blade profile, ε, β and x_c/c. Figure 5 shows a schematic of the turbine mounted in the wind tunnel test section. It consists of a vertical shaft, two pairs of variable-length horizontal struts, and vertically mounted blades. The shaft was mounted on two low-friction, self-aligning bearings fixed above and below the test section.

For all experiments, a two-bladed configuration was employed, with either NACA 0012 or NACA 0021 blade profiles, with chord and span dimensions $c = 300$ mm and $h = 970$ mm, respectively. They consisted of internal load-bearing spars, three aluminum ribs, and 3D-printed PLA shells, 1.5 mm thick, that were screwed to the ribs. The surfaces of the blades were sandpapered, primed, and painted to a smooth finish. Gaps of 15 mm between the tunnel floor or ceiling and the blade edges reduced losses due to tip vortices [35]. Blade ribs (aluminum 6061-T651) corresponding to the strut locations, were equipped with threaded sections that allowed strut attachment locations on the range $0.24 \le x_c/c \le 0.72$. The struts were constructed with rounded rectangular cross-sections of $10\text{ mm} \times 30\text{ mm}$ (4340 steel, AMS 6359), and bolted to the aluminum shaft (diameter $d = 50.8\text{mm}$) using adapter plates. A combination of strut elements was used to vary the turbine radius R, from 250 mm to 500 mm in steps of 50 mm, to achieve $0.6 \le \varepsilon \le 1.2$ $(1.2 \le \sigma \le 2.4)$, with a turbine projected area to the test section area blockage ratio of $0.25 \le BR \le 0.5$. Pitch angle variations were achieved employing precise slanted strut ends, for $-10° \le \beta \le 10°$.

All evaluations were performed in a low-speed blower-type wind tunnel [36], modified to a larger test section of dimensions $1900\text{ mm} \times 1004\text{ mm}$. The length of the test section was 3850 mm, and the turbine shaft was located at its center. Two 50% solidity screens were placed between the contraction and the test section to increase flow uniformity. Hot wire anemometer and pitot-tube measurements at 1,500 mm downstream of the screen, showed a relative standard deviation $\sigma_{U_\infty}/\bar{U}_\infty = 1.4\%$ and turbulence intensity $Ti = 0.5\%$. Experiments were performed at nominal wind speeds in the range of $1.0\text{ m/s} \le U_{\infty,\text{nom}} \le 4.5\text{ m/s}$, whereas the majority of the experimental data was obtained at nominal wind speeds of $U = 2.8\text{ m/s} \pm 0.15\text{ m/s}$. Since the velocity relative to the blade changes along the rotation and the chord, the corresponding blade's average Reynolds number, defined as $\overline{Re_c} \equiv \omega_{\text{opt}} Rc/\nu$

[34], where ω_{opt} is the rotational speed obtained at λ_{opt}, was used in this study. For the majority of the experiments, the average Reynolds number obtained was $0.6\times10^5 \le \overline{Re_c} \le 1.8\times10^5$.

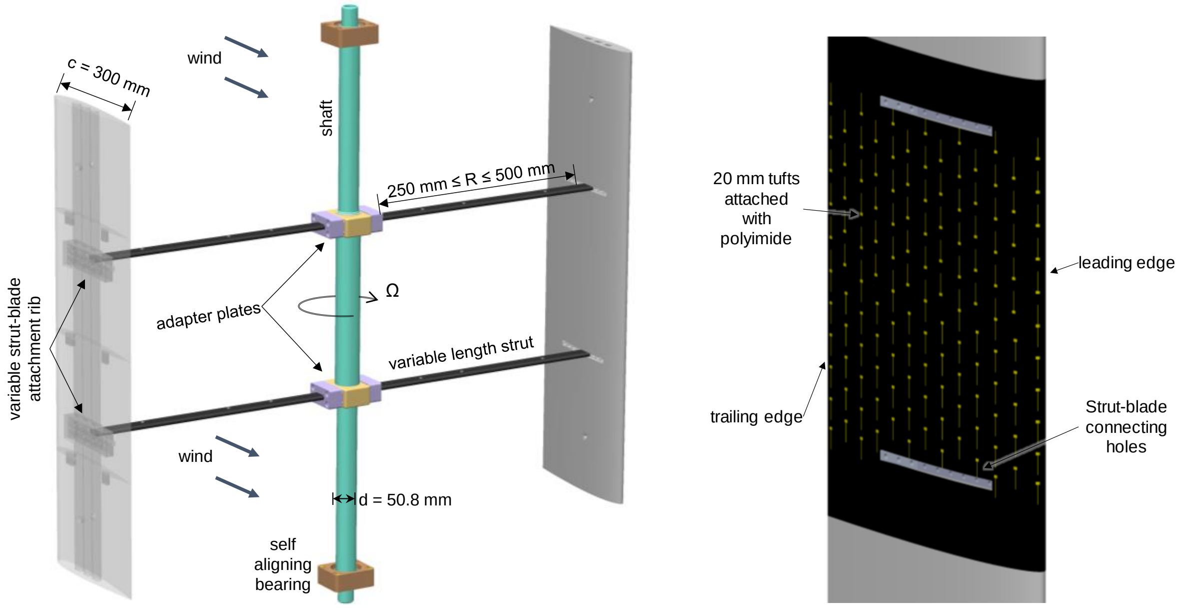

Figure 5: (Left) Blade configuration and strut-connection schematics, with one element rendered transparent (Right). Schematics of the tuft grid on the turbine blade, located mid-span.

3.2 Data Acquisition

Tunnel velocity was measured 2,000 mm upstream of the turbine shaft for all experiments, employing two pitot-static probes connected to two Siemens QBM3020-1U 50 pascal pressure transducers. In addition, the velocity distribution was measured upstream and downstream of the turbine for various operation points, validating the measured wind speed. Power was measured employing a dynamometer comprising a Kistler 4502A10RAU 10 ± 0.02 Nm, torque/rotational speed transducer, and an HB-140M2 Magtrol 10 Nm hysteresis magnetic brake connected through flexible couplings.

The system was controlled using a dedicated programmed LabVIEW© program. The program controlled the dynamometer back-torque automatically via a TTI CPX400DP programable power supply while acquiring real-time measurements from the various sensors. The load torque was varied in steps of $0.005\mathrm{Nm} \le \Delta T \le 0.02\mathrm{Nm}$, and data was acquired for 60 to 240 seconds as the rotational speed reached a steady-state, defined as $c_v < 0.002$, where $c_v = \sigma_\omega / \bar{\omega}$; σ_ω is the standard deviation and $\bar{\omega}$ is the time-average ω. The average time of each experiment was approximately 120 minutes. Due to the large blockage ratio, the data obtained was corrected using a dedicated high blockade VAWT wind tunnel correction based on Kinsey and Dumas [37], yielding corrected wind speed, U_{corr}, which will be referred to in the following sections as U_{∞}.

3.3 Flow Visualization

Tuft-based flow visualization was performed by placing a tuft grid on the inboard part of a single-blade midspan. The grid measured 300 mm × 320 mm and consisted of 143 white polyester fluorescent tufts, 40 m/g (wt.) thick and 20 mm long. The tufts were spaced at an average distance of 30 mm from each other and placed, directing vertically downwards and upwards, normal to the flow direction (see Figure 5, right). This orientation reduced the influence of the high centrifugal forces by increasing their sensitivity to velocity changes in the direction of the chord. They were attached to a matte black base and glued using a 3 mm × 4 mm, 75 μm thick polyamide tape to maintain a high contrast with the matte black base. The grid was illuminated by means of a 180W UV fluorescent cannon, and recording was performed using a high-speed Phantom v7.3 camera at 3,000 frames per second.

4 Result and Discussion

In order to investigate the performance of the DSDT, an extensive parametric investigation was performed, including profile shape, ε (or σ), β, x_c/c and $Re_{c,\lambda} \equiv U_\infty c(1+\lambda)/\nu$. Flow visualization experiments were also performed to elucidate the flow-field over the blades. The scope of the study is summarized in Table 1. For all experiments, the unloaded turbine was spun up unaided until reaching a constant maximum rotational speed (ω_{max}), corresponding to $\lambda_{max} \equiv \omega_{max} R/U_\infty$. The turbine was then gradually loaded to obtain successive steady-state operation conditions for the full λ range, as described in section 3.2. The results were evaluated on the basis of power and torque coefficients, namely:

$$C_P \equiv \frac{P}{\frac{1}{2}\rho A U_\infty^3} \tag{13}$$

and

$$C_T \equiv \frac{T}{\frac{1}{2}\rho R U_\infty^2 A} \tag{14}$$

where $P \equiv T\omega$ is turbine power, T is the shaft torque, ρ is the air density and $A \equiv hR$ is the turbine projected area. All the experimental results presented in this chapter were corrected for wind tunnel blockage effects, according to the method described in [37].

Table 1: Summary of test cases and parameters varied for the parametric study.

Test Case	Profile	c/R (ε)	Solidity (σ)	Preset pitch (β)	Blade offset x_c/c	Wind speed (U_∞)
	-	-	-	[deg]	-	[m/s]
Impact of ε	NACA 0012 NACA 0021	0.6 - 1.2	1.2 - 2.4	0	0.48 0.51	2.8
Impact of β	NACA 0012 NACA 0021	0.6 - 1	1.2 - 2	-8 - 8	0.48 0.47, 0.51	2.8
Impact of x_c/c	NACA 0012 NACA 0021	0.6 - 1	1.2 - 2	0	0.36 - 0.66	2.8
Impact of Re number	NACA 0012 NACA 0021	0.75	1.5	0	0.48 0.51	0.8 - 4.2 2.8 - 4.7
Flow visualization	NACA 0012 NACA 0021	0.6, 0.75	1.2, 1.5	0	0.48 0.51	2.8

4.1 Effect of Blade Profile Chord-to-Radius Ratio

Figure 6 shows the influence of the chord-to-radius ratio, ε, on performance for both NACA 0012 and 0021 profiles connected chord mid-chord (zero offset) with $\beta = 0°$. The turbine attains maximum power coefficients of $C_{P,max} \approx 31\%$ and $C_{P,max} \approx 17\%$ for the NACA 0021 and the NACA 0012, respectively. These high maximum power coefficients were attained at a corrected chord-based Reynolds number of $\overline{Re_c} < 10^5$. The maximum power coefficients obtained with NACA 0021 blades are comparable to those obtained by commercially-available large-scale VAWTs [4] and greater than those of conventional multibladed high-solidity and low-solidity machines at corresponding Reynolds numbers [10,38,39]. Furthermore, the operational speeds are relatively low, in the $0.8 \leq \lambda \leq 2.25$ range. Thus, the DSDT produces power coefficients comparable to lift-based machines with rotational speeds comparable to drag-based machines. The combination of high-power coefficients and low rotational speeds is highly desirable for urban wind turbine applications. Furthermore, the attainment of these conditions at low Reynolds numbers is particularly advantageous for applications in low wind speed environments.

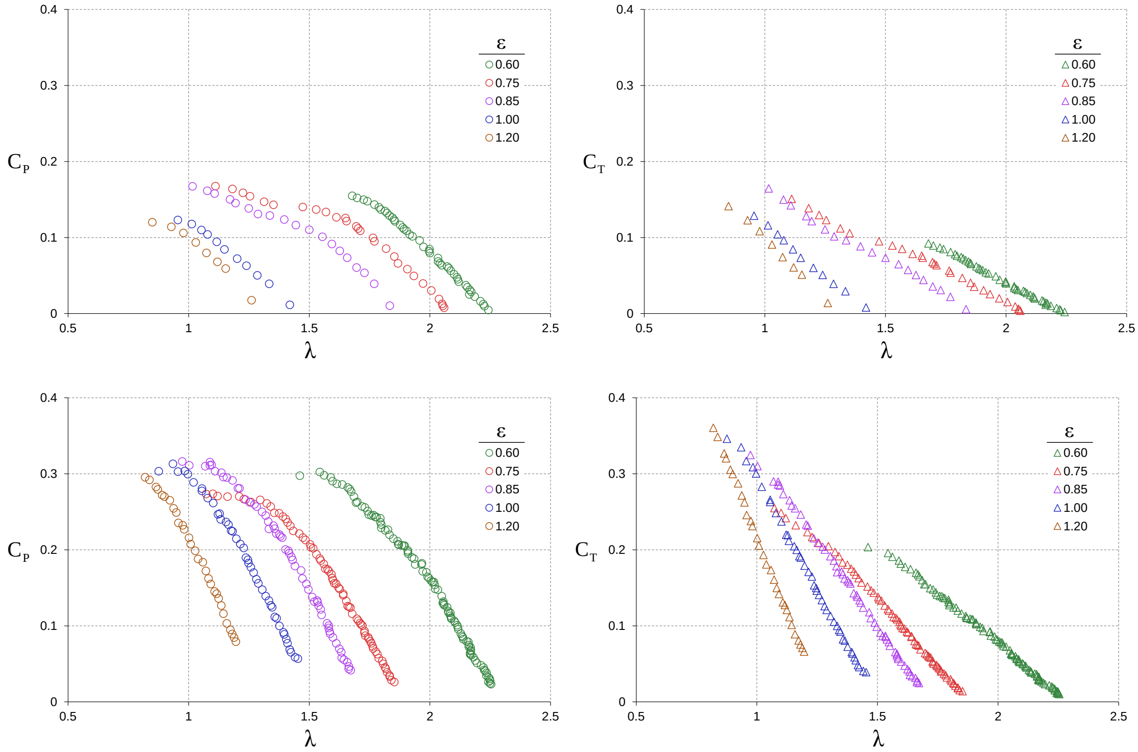

Figure 6: Effect of chord-to-radius ratio on turbine performance at $U_\infty = 2.8$ m/s and $\beta = 0^\circ$: power and torque coefficients as a function of tip speed ratio (left and right); NACA 0012, $x/c = 48\%$ (top row); NACA 0021, $x/c = 51\%$ (bottom row).

The differences between the NACA 0012 and NACA 0021 power and torque coefficients are considerable, with the latter greater by almost a factor of two. The NACA 0012 airfoil has low parasitic drag, but even at low Reynolds numbers, it is a “leading-edge staller,” meaning that stall is controlled mainly by bursting of the leading-edge bubble, resulting in a sharp loss of lift at post-stall angles [40]. Under dynamic conditions, a large lift overshoot is due to the formation of a leading-edge vortex (LEV) [41]. In contrast, the NACA 0021 has a slightly larger parasitic drag, while flow separation commences at the trailing-edge and creeps upstream with an increasing angle of angle of attack. At low Reynolds numbers, this results in a higher $C_{l,\max}$ and gentle stall behavior with only a small loss of lift at post-stall angles [31,42–45]. Under dynamic conditions at large angles of attack, thick airfoils produce a vortex on the rear half of the blade, termed the aft dynamic stall vortex (ADSV), that corresponds to a lift overshoot [19]. It is a clearly distinct vortex, and its formation and shedding precede that of the conventional leading-edge vortex, while its strength increases with increasing κ. This ADSV appears to be the primary mechanism producing the high values of power coefficient. Thus, in contrast to conventional turbine operation, the *post-stall* performance has a dominant effect on turbine power. This fundamental difference indicates that conventional blade profiles and design tools are unsuitable for analyzing and designing dynamic-stall-driven turbines.

Compared to other studies, a notable difference is that the results contain only the "right side" of the power curve, $\lambda > \lambda_{\text{opt}}$, where λ_{opt} corresponds to $C_{P,\max}$. The absence of the left side of the power curve is due to the turbine loading method, comprised of a hysteresis break with no angular speed control [25,46,47], and this matches the results of studies that employed similar loading and sensing systems [48–52]. Therefore, when using a purely resistive load like a brake or a fluid pump [14], the operational stability is delineated as "stable" (namely $\lambda > \lambda_{\text{opt}}$) and "unstable" (namely $\lambda < \lambda_{\text{opt}}$). When the turbine operates in the stable region, a slight increase in loading slows the turbine, accompanied by an increase in the C_P, resulting in a new operating point. A slight decrease in loading causes the opposite effect. However, if the turbine is overloaded and no speed control is implemented, the turbine operation becomes unstable. Thus, the main limitation of a resistive load is that overloading the system may arrest the turbine, and feedback is required to return the turbine to a stable operating regime.

Figure 6 shows that the peak power coefficients are weakly dependent on ε and that the corresponding optimal speed ratios λ_{opt} for the different profiles are similar. Thus, apart from the highest NACA 0012 solidities, the dynamic stall mechanism renders the turbine almost independent solidity, irrespective of the dynamic stall mechanism, i.e., leading-edge versus trailing-edge. This should be contrasted with studies that show a decrease in power coefficient with the increase in solidity by increasing the number of blades [10,48,49]. This effect is often associated with a decrease in Reynolds number, attributable to the decrease in the operational λ, but Miller et al. [49] determined that it is Reynolds number independent.

Thus, there is a fundamental difference between increasing σ through N or ε. In the latter case, the dynamic stall mechanism ensures virtually no change in the peak power coefficient in the range $0.5 \le \varepsilon \le 1.2$. A similar observation was made in a numerical study by [11]. One interesting outlier is the relatively low NACA 0021 power coefficient at $\varepsilon = 0.75$. Without surface pressure or flow-field measurements, no credible reason can be given for this. It should be noted, however, that a small decrease in the blade offset and an increase in the pitch angle β remove this anomaly (see section 2).

As discussed in section 2, both the dimensionless pitch-rate κ and the maximum virtual camber $z'_{\max}$ are linearly dependent on ε. Both of these factors affect the dynamic stall process, and hence the turbine power. It is well known that, on airfoils, increasing the pitch-rate delays dynamic stall to higher angles-of-attack [8,27,53,54], whereas increasing camber increases lift at the expense of higher drag [45]. Hence, on the turbine, increasing ε has a similar effect, resulting in larger driving torque. This reasoning is consistent with the study of Buchner et al. [55], who show that the spatial extent of the leading edge vortex varies inversely with pitching rate, where an increased LEV spatial extent is associated with an earlier shedding of the vortex. On the other hand, excessive virtual camber, namely $z'_{\max} > 5\%$, causes flow separation from the outer high-pressure surface, thereby reducing turbine's torque. These two opposing mechanisms seemingly offset one another; hence, the net result is a weak dependence on ε.

From an applications perspective, the high-power coefficients and large operation range for $0.74 \le \varepsilon \le 0.85$ have mainly favorable implications. This is because the relatively low operational λ reduces blade noise, reduces centrifugal forces on the blades and drivetrain, and poses less danger to birdlife. However, larger ε results in a smaller swept area for a given blade chord length, resulting in a possible small power output (see eqn. (13)). Therefore, further study is required to investigate the economic feasibility of the DSDT for urban use.

4.2 Effect of Preset Pitch Angle, β

This section investigates the effects of the preset pitch angle β on turbine performance. Figure 7 summarizes the main results, namely $C_{P,\max}$, $\lambda_{\max}$ and λ_{opt} for both profiles with approximately zero offset at several ε. Positive and negative β denote pitch-up and pitch-down angles, respectively (see Figure 3). Peak NACA 0012 and NACA 0021 $(\varepsilon \ne 0.75)$ is attained at $\beta \approx 0°$ and this should be contrasted with studies that showed performance increases for $\beta \ne 0$ [26,56–59]. For example, [56] and [57] recommend negative preset angles of $\beta = -2°$, while other studies [26,58,59] suggest positive preset angles for performance enhancement. However, the anomaly attained for the NACA 0021 at $\varepsilon = 0.75$ is consistent with these latter findings, where peak performance is attained in the range $2° \le \beta \le 4°$.

Furthermore, consider these data with the blade offset-preset angle arguments presented in section 2.3. According to eqn. (8), a similarity exists because the x_c / c reduction produces less virtual camber at the leading-edge, corresponding to a greater virtual preset angle. Some studies [56,57] report performance increases at negative preset angles due to a strut-blade offset from the mid-chord towards the leading edge, often to the quarter chord. Thus, adverse effects of strut-blade connection at the quarter chord can be canceled out by a negative β, as implied by eqn. (8).

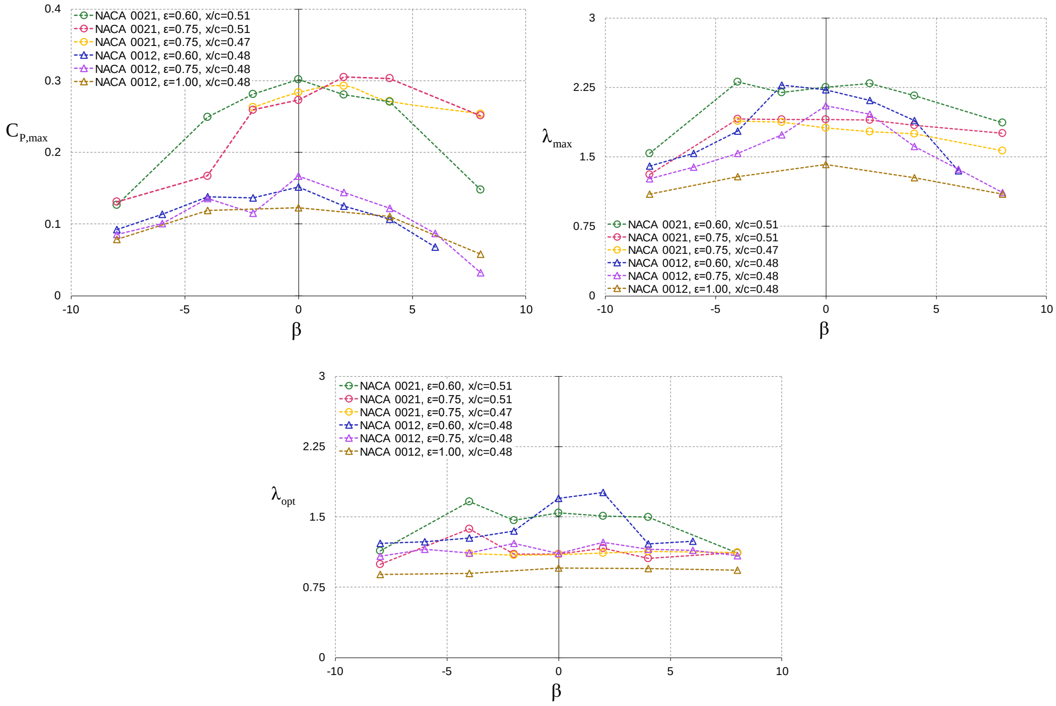

Figure 7: The effect of preset pitch angle on the main turbine performance parameters for three ε values at $U_\infty = 2.8$ m/s. NACA 0012: $x/c = 48\%$; NACA 0021, $x/c = 51\%$.

Although an apparent similarity exists between the effect of positive and negative preset angles in Figure 7, positive angles produce slightly greater adverse and beneficial effects for the NACA 0012 and 0021, respectively. These qualitative differences are due to differences in the dynamic stall mechanism. For the relatively thin NACA 0012, increasing β increases the angle of attack, which results in an earlier appearance and shedding of the DSV [26,56]. Although the earlier appearance of the DSV at higher dynamic pressures increases the maximum tangential force, it reduces the azimuthal arclength over which the turbine produces useful torque. In contrast, negative β decreases α during pitch-up, thereby delaying the DSV formation and shedding at lower dynamic pressure, resulting in a lower maximum lift [26]. Additionally, in the downwind quadrants, negative β is typically associated with an increase in torque coefficient for high-solidity VAWTs [26,56], whereas positive preset is associated with a decrease in torque. The cumulative effect leads to a reduction in performance for both negative and positive preset angles, with a smaller net deleterious effect on turbine torque, to some extent, for negative angles. Since the impact of β on performance is in part produced by the shift in θ_{stall}, higher ε turbines are less susceptible to preset variations as they operate at a larger range of α 's and are less impacted by a fixed change in α across the operational range. This results in a higher impact of β on the turbine performance for lower ε turbines, as seen in Figure 7. In addition, of particular importance is the relatively large power coefficient sensitivity to small changes in preset angle for the NACA 0021 than for the NACA 0012. For example, for $\Delta\beta = -6°$ at $\varepsilon = 0.75$, the reduction of $C_{P,\max}$ for the NACA 0021 and NACA 0012 (see Figure 7), is $\Delta C_{P,\max} = 45\%$ and $\Delta C_{P,\max} = 25\%$, respectively.

Similar to the effect on $C_{P,\max}$, the impact of β on $\lambda_{\max}$ is roughly equal for both positive and negative β, for the NACA 0012, with a more substantial influence for positive preset angles. At $\lambda_{\max}$, the loading on the blades turbine is minimal, suggesting that the profile with the smallest integral drag coefficient $\left(\int_0^{2\pi} \mathrm{C}_d \, d\theta\right)_{\min}$, namely the NACA 0012, will produce the higher $\lambda_{\max}$, as shown in Figure 7. However, counterintuitively, for the NACA 0021, $\lambda_{\max}$ is unaffected by small blade pitching of $-4° \le \beta \le 4°$. This suggests that small preset angles have a negligible effect on the overall drag of the blade along the turbine rotation. Additionally, from Figure 7, we may conclude that λ_{opt} is virtually independent of the preset angle. This corresponds to the study of [58], indicating constant λ_{opt} for several preset angles for a medium solidity turbine with symmetrical blades. Therefore, the above denotes a decrease in the operational tip speed ratio range, $\Delta\lambda_{\text{range}}$ with the increase in $|\beta|$. Consequently, we can summarize that an increase in the absolute value of the preset angle for a turbine connected mid-chord is associated with (i) a loss of performance; (ii) a decrease in $\lambda_{\max}$; (iii) a reduced operational tip speed ratio range, $\Delta\lambda_{\text{range}}$; and (iv) an invariance to λ_{opt}. Furthermore, these influences increase for lower ε turbines.

4.3 Effect of Blade Offset, x_c / c

Figure 8 shows the effect of the strut-blade connection point, x_c / c on the performance of the DSDT. As discussed previously, any variation in the strut-blade connection point transforms the virtual camber of the airfoil [24], as seen in eqn. (4). The impact of blade offset can also be addressed separately from the blade's virtual cambering, as the virtual pitch, β_{vir}, as indicated by eqn. (8). As mentioned in section 2, although frequently overlooked in VAWTs, the effect of blade offset has a significant impact on higher ε turbines and, therefore a leading parameter affecting the performance of DSDTs. For example, when $\varepsilon = 0.75$, a 2% of chord offset ($\Delta x = 6$ mm in our study) produces a virtual pitch of $\beta_{\text{vir}} = 0.4°$, compared to $\beta_{\text{vir}} = 0.06°$ for a comparable VAWT with a $\varepsilon = 0.1$. This elucidates why high solidity VAWTs with symmetrical blades, often experience a performance degradation if not connected mid-chord but at the conventional quarter-chord, attributable to the symmetrical airfoil's moment stability.

Similarly to β, an offset from the mid-chord has, to some extent, a symmetrical impact on $C_{P,\max}$ and $\lambda_{\max}$, with a more adverse effect for $x_c / c < 0.5$ (positive β_{vir}). In addition, the tip speed ratio at peak power, λ_{opt}, is also independent of the pitch angle. In the previous section, it was shown that the impact of β decreases with the increase in ε. However, despite this similarity, increasing ε produces a more significant influence on the turbine's performance for comparable blade offset, $\Delta x_c / c \equiv \tfrac{1}{2} - \tfrac{x_c}{c}$; as can be deduced from eqn. (8).

Besides the virtual preset angle, blade offsetting has an additional effect on the aerodynamic characteristics of the blade via the axis of rotation. Even though the expression for κ in eqn. (11) was developed for the x_c / c location, it is representative of conditions along the entire chord length, κ'. This can be seen by replacing θ in eqn. (11) with $\theta + \beta'$, which shows that at small angles $\kappa' \approx \kappa$, as both the local pitch rate $\dot{\alpha}' \equiv d\alpha'/dt$ and the relative velocity $|W'|$ vary similarly. By the same token, variation of x_c / c away from mid-chord has a very small effect on κ'. Nevertheless, it has been shown that for a NACA 0015 airfoil at a constant pitch-rate, the *pitch axis* does affect airfoil performance [60], because the local velocity normal to the chord, changes. For $x_c / c < 1/2$, the relative velocity vector, normal to the leading edge, decreases while the velocity normal to the trailing edge, increases, and vice versa for $x_c/c > 1/2$. These variations in the velocity, normal to the chord, change its apparent camber [60]. The net result is that the pitching of symmetrical blades around $x_c/c < 1/2$ results in reductions in $\Delta\alpha_{\mathrm{stall}}$ and $C_{L,\max}$. This pitch axis effect is a credible explanation of why turbine performance reduces more for $x_c/c < 1/2$, than for $x_c/c > 1/2$; a trend exists for the NACA 0012, as shown in Figure 8. However, for the NACA 0021, pitching closer to the trailing edge results in a more positive effect than $x_c/c < 1/2$. This may be because additional virtual cambering is adverse and may result in an earlier shedding of the DSVs for thick airfoils. It also may be that the increase in the relative velocity near the trailing edge, for $x_c/c < 1/2$, has a beneficial impact on the ADSV and is only present on thicker airfoils.

Although it was previously hypothesized [7] that a blade offset alters the virtual camber to produce an apparent nose droop, the data obtained in this study supported the virtual pitch and pitch-axis hypotheses. Comparing the results shown in Figure 7 and Figure 8, we can deduce that blade offset is roughly analogous to a virtual pitch. This means that offsetting the strut-blade connection point, x_c/c, produces an approximately analogous effect as virtually pitching the blade by β_{vir} (as defined in section 2).

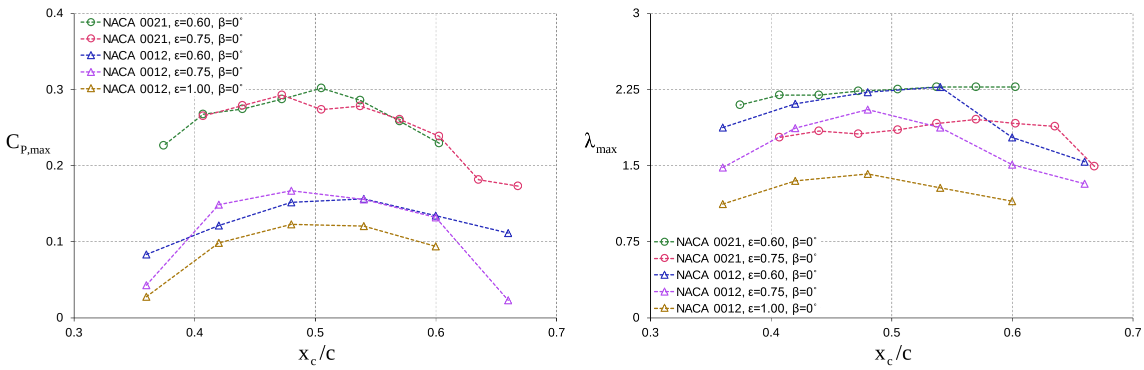

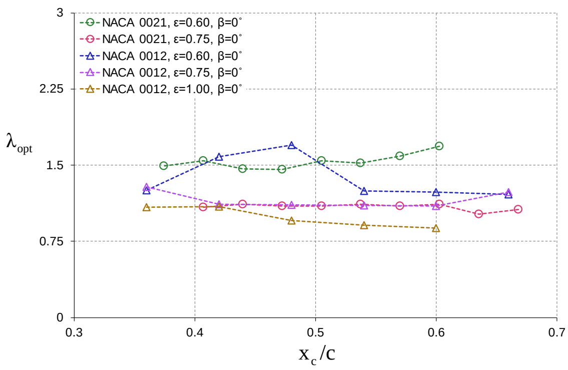

Figure 8: Impact of the strut-blade connection point, x_c / c, on the DSDT (top left) C_P (top right) $\lambda_{\max}$ (bottom) λ_{opt}. For three ε and $\beta = 0^\circ$, $U_\infty = 2.8$ m/s.

To summarize, an increase in the offset of the strut-blade connection from the mid-chord is associated with (i) a loss of performance; (ii) a decrease in $\lambda_{\max}$; (iii) a reduced operational tip speed ratio range, $\Delta\lambda_{\text{range}}$; and (iv) λ_{opt} invariance.

4.4 Effect of Reynolds Number, $\overline{Re_c}$

Figure 9 presents the impact of wind speed, or effectively, the influence of Reynolds number on the DSDT performance for a single chord-to-radius ratio of $\varepsilon = 0.75$ (similar results obtained for $\varepsilon = 0.6$). The influence of the Reynolds number on thin symmetrical NACA airfoils at $10^4 < Re_c < 10^6$ is substantial due to their poor performance at low Reynolds numbers. For a NACA 0012, lift and stall angle increase by ~50% when increasing the Reynolds number from $Re_c = 10^5$ to $Re_c = 10^6$, in addition to a substantial decrease in $C_{D,0}$ [44,45]. Since the average chord-based Reynolds numbers obtained in the previous sections are relatively low, namely $\overline{Re_c} \equiv \omega Rc / \nu \approx O\left(10^4\right)$, this increase in the turbine performance was anticipated.

From Figure 9 (left), it can be seen that an increase in Reynolds number by 50% produces an increase in $C_{P,\max}$ of 12.5% in for the NACA 0012 blades, in addition to the increase of operational tip speeds, $\lambda_{\max} - \lambda_{opt}$. In contrast to traditional small-scale wind turbines, which typically struggle to generate positive torque at very low speeds and Reynolds numbers [13,61], the DSDT proves effective in producing torque even at wind speeds as low as $U_\infty \approx 0.8$ m/s. This is partially attributable to the atypical forces driving the turbine at these relatively low Reynolds numbers. Based on Miller et al. [49], scaling the system's Reynolds to

$Re_c = 10^6$ should produce an increase of more than 50% in $C_{P,\max}$ compared to performance acquired at a nominal wind speed of $U_\infty = 2.8$ m/s. Although the NACA 0021 outperformed NACA 0012 at this range of Reynolds numbers, this may not be the case at significantly higher Reynolds, where the latter produces the best performance [62]. Therefore, the authors estimate operational performance coefficients of $C_{P,\max} \to 30\%$ for a mid-scale DSDT operating with NACA 0012 blades.

In contrast to the NACA 0012, Figure 9 (right) shows that the variation of Reynolds numbers with NACA 0021 blades had almost no effect on $C_{P,\max}$. The reason for this is that the post-stall lift coefficient is significantly affected (improved) for the NACA 0012, while it is only marginally affected for the NACA 0021 [44,45]. The almost constant NACA 0021 $C_{P,\max}$ reflects observation.

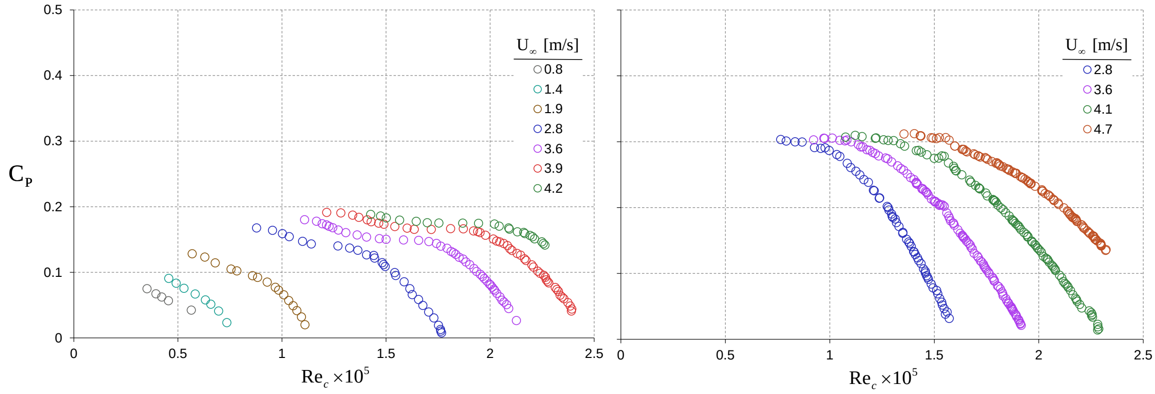

Figure 9: Impact of $\overline{Re_c}$ on the DSDT's performance for (left) NACA 0012 (right) NACA 0021. $\varepsilon = 0.75$, $\beta = 0^\circ$, and $x_c / c = 0.48$ for all experiments.

4.5 Flow Visualization

Tuft visualization was performed for both blade profiles at $\varepsilon = 0.6$ and $\varepsilon = 0.75$ at successively lower values of λ corresponding to increasing turbine power (see Figure 10). In order to provide a common basis for comparing the two blade profiles, we define the dimensionless quantity $\zeta \equiv (\lambda - \lambda_{\min}) / (\lambda_{\max} - \lambda_{\min})$. For the NACA 0012, when the turbine is unloaded at $\zeta = 1$, the tufts indicate almost completely attached flow, with minor leading-edge separation at $\theta = 180°$, when $\varepsilon = 0.75$. As the turbine is gradually loaded, evidence of leading-edge flow separation appears, which is indictive of the formation of an LEV. The greater degree of separation observed at $\varepsilon = 0.75$ is a combined result of higher angles-of-attack and higher pitch-rates. As the turbine approaches peak power, corresponding to $\zeta \to 0$, formation of the

LEV is observed at successively lower azimuthal angles θ. Ultimately, at peak power ($\zeta = 0$), LEV formation is observed at $\theta = 90°$ and $\theta = 45°$ for $\varepsilon = 0.6$ and $\varepsilon = 0.75$, respectively. Note that virtually no evidence of trailing-edge separation is visible, with the exception of $\theta = 180°$ and $135° \leq \theta \leq 180°$ for $\varepsilon = 0.6$ and $\varepsilon = 0.75$ respectively. This is fully consistent with our hypothesis that peak power is attained when the shedding of the vortex occurs at low relative dynamic pressures.

The NACA 0021 images show an entirely different dynamic stall mechanism to that described above, and, as hypothesized, the trailing-edge plays a dominant role. In fact, even with the turbine unloaded, there is evidence of incipient aft separation in the first quadrant ($\theta = 45°$) for $\varepsilon = 0.75$. This separated flow is detectable throughout the range of upstream azimuthal angles. As expected with increased loading, separation in the first quadrant on the aft of the blade becomes successively more pronounced. Similar observations are made for $\varepsilon = 0.6$, but at smaller values of ζ. Under greater loading and larger azimuthal angles, leading-edge separation indicates a leading-edge vortex. The flow visualization images can be interpreted as follows: As the blade pitches up, a distinct ADSV is formed that is initially responsible for the overshoot in lift and hence, turbine power. With further increase in the angle-of-attack, a conventional leading-edge vortex (LEV) is formed, further producing a power increment. Higher pitch rates produced by higher ε results in stronger ADSVs and LEVs, with the net result of higher turbine power. These conclusions, based on thick airfoil dynamic airfoil experiments as described in section 2.1 and [19], are fully consistent with the flow visualization images.

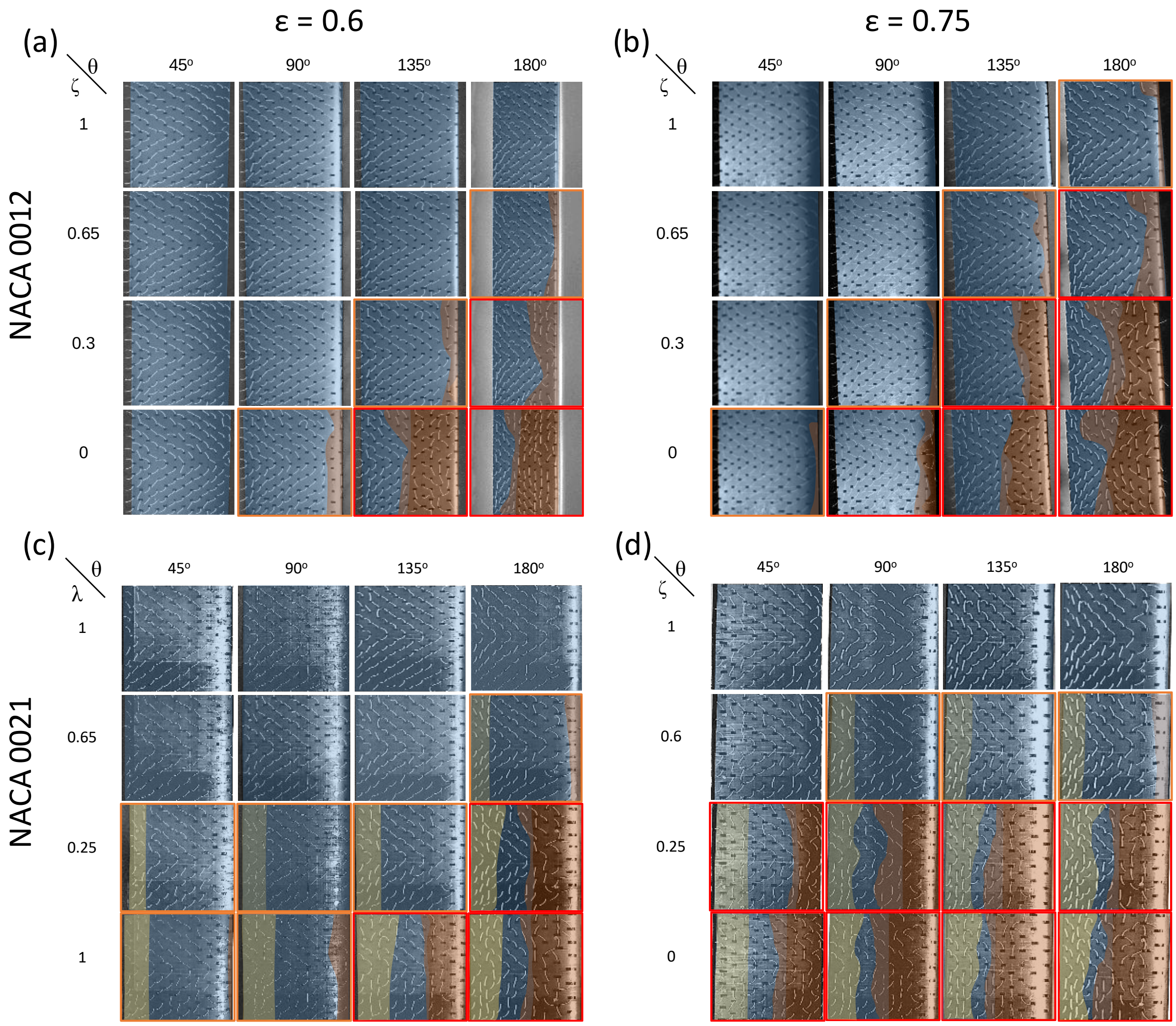

Figure 10: Inboard tuft-based flow visualization on the NACA 0012 and NACA 0021 for $\varepsilon = 0.6$ and $\varepsilon = 0.75$ [$U_\infty = 2.85, \beta = 0^\circ$, $x_c / c = 0.48$ (NACA 0012), $x_c / c = 0.51$ (NACA 0021)]. Background color code: blue: attached flow; orange: appreciable streamwise component and; red: separated leading-edge flow; yellow: trailing-edge separation. Red and orange outlines represent an appearance of deep stall and LE separation of the blade, respectively.

4.6 Economic and Market Considerations

Small-scale, distributed renewable energy systems are gaining greater prominence, particularly in regions without electrical grid connections. Thus, the potential of small wind turbines in the urban, rural, and off-grid wind-energy landscape is significant, and the global small wind turbine market is witnessing significant growth, with over 1 GW of installed capacity [3]. This represents a unique opportunity for DSDTs due to their simple design, high efficiency, low rotational speeds, and ability to operate in lower windspeed environments, discussed below.

The future economic potential of DSDTs lies in their suitability to the evolving market needs. Their design, advantageous for low noise emission and reduced bird life impact [15,16], makes them particularly suitable for rural and urban environments, aligning with modern ecological and societal demands. The structural integrity and efficiency of DSDTs, stemming from their large chord-to-radius ratio, provide a solid economic argument for using VAWTs, that frequently tend to fail due to structural integrity. DSDTs offer greater torque and self-starting capabilities, crucial for high-pressure applications like irrigation [14] and desalination systems [63], which are often a part of off-grid rural setups. The high efficiency at lower Reynolds numbers and wind speeds, a typical challenge for conventional, lift-based wind turbines, broadens the scope of DSDTs to areas with varying wind conditions, thus increasing their market applicability [64]. With increased public awareness and acceptance of wind energy and an increasing focus on sustainable living [65], DSDTs could cater to a range of applications beyond conventional energy generation, such as integration into renewable-based agricultural infrastructure or as part of community-based renewable energy projects.

Looking forward, the economic potential of mass manufacturing of the DSDT should be studied together with the first field implementation of the DSDT. However, the economic scope of DSDT should also be viewed through the lens of policy and market acceptance [66]. As global initiatives towards sustainable energy gain momentum, policy measures favoring distributed and urban renewable energy technologies are likely to influence the adoption of the DSDT substantially. Moreover, the recent implementation of policies aimed at fostering decentralized and microgrid energy systems could pave the way for expanded market opportunities, especially in regions with non-existent grid infrastructure. In conclusion, as the renewable energy sector continues to evolve, and the public and governmental acceptance of small-size wind turbines increases, the DSDT can stand out as a promising technology, offering both simple design and economic feasibility, particularly in urban and off-grid settings.

5 Conclusions

In this paper, an experimental study was conducted on a small-scale, two-bladed, H-rotor, dynamic stall-driven vertical axis wind turbine (DSDT), where five main parameters were varied, namely: (i) the chord-to-radius ratio ε; (ii) the preset angle β; (iii) the chord-strut connection (offset) point x_c / c; (iv) the airfoil thickness (i.e., NACA 0012 and NACA 0021); and (v) the Reynolds number. Additionally, the main factors impacting the DSDT performance were discussed and explained.

In contrast to low solidity turbines, the peak power coefficients were virtually independent of chord-to-radius ratio in the range $0.6 \le \varepsilon \le 0.85$ and were attained in the range $0.8 \le \lambda \le 1.6$. At low Reynolds numbers, $\overline{Re_c} \approx 0.8 \times 10^5$, the turbine performance with NACA 0021 blades was vastly superior to that with NACA 0012 blades, producing $C_{P,\max} \approx 0.31$ and $C_{T,\max} \approx 0.32$ at $\lambda \approx 1$ with $\varepsilon = 0.85$. These values were approximately 90% greater than those obtained using NACA 0012 blades. This combination of high power coefficients and low rotational speeds is highly desirable for urban wind turbine applications. Furthermore, the corresponding low Reynolds numbers render DSDTs directly applicable to low wind speed environments or as small-scale wind power systems. Tuft-based flow visualization showed substantial differences between the stall mechanisms on the different blades. On the NACA 0012, increased loading of the turbine produced greater leading-edge separation indicative of the formation and shedding of a leading-edge vortex (LEV). On the NACA 0021, trailing-edge separation played a dominant role, where increased loading showed increasing trailing-edge separation, prior to leading-edge separation. This was interpreted as the formation of an aft dynamic stall vortex (ADSV) that is formed and shed prior to the formation and shedding of the LEV.

Peak performance was attained with the blade preset angles close to $\beta \approx 0°$. The similar reductions in performance for $\beta > 0°$ and $\beta < 0°$ were attributed to differences in the dynamic stall mechanism. For $\beta > 0°$ the angle-of-attack increases, which results in earlier appearance and shedding of the DSV. Although the earlier appearance of the DSV at higher dynamic pressures increases the maximum tangential force, it reduces the azimuthal arclength over which the turbine produces useful torque. In contrast, $\beta < 0°$ decreases the angle-of-attack, thereby delaying the DSV formation and shedding at lower dynamic pressure, resulting in lower maximum lift and hence less torque.

Much like the preset angle results, peak performance was attained at a blade offset of $x_c / c \approx 1/2$. This effectively validated the relationship between the blade preset angle and the virtual preset angle, where a deviation from the strut-blade mid-chord connection point, $x_c / c = 0.5$, resulted in a virtual preset angle, β_{vir}. The poorer performance observed at $x_c / c \neq 1/2$ was explained similarly to the impact of the blade preset angle, with an additional effect due to the variation in the pitch rate. In particular, at $x_c / c < 1/2$ the blade experiences a lower relative velocity normal to the leading edge, leading to decreases in $\Delta\alpha_{\mathrm{stall}}$ and $C_{L,\max}$.

The Reynolds number effects for the two blade profiles, examined in the range $0.35\times10^5 \leq Re_{c,\lambda_{\mathrm{opt}}} \leq 1.4\times10^5$, were significantly different. In the case of the NACA 0012 blades, $C_{P,\max}$ increased by 12.5% for a 50% increase in Reynolds number. In contrast, almost no effect was observed with the NACA 0021 blades. This was attributed to significant *post-stall* lift coefficient increases for the NACA 0012 airfoil and only marginal increases for the NACA 0021. Nevertheless, significant performance improvements can be anticipated for $Re_c \sim 10^6$.

Future DSDT research should focus on three-bladed configurations and blade profile optimization. Because only the upwind quadrants generate useful torque, asymmetric profiles should be considered. In addition to conventional airfoil performance metrics, such as high maximum lift coefficient and aerodynamic efficiency, a large positive-lift angle-of-attack range and gentle stalling characteristics are major design requirements, particularly in the presence of inevitable blade fouling. Furthermore, since this is an unexplored design space where conventional techniques are of little use, phase-resolved surface pressure and flow-field measurements, e.g., particle image velocimetry (PIV) should be performed. In addition, high-fidelity computational tools should be used to gain a deeper understanding of the DSDT physics and the aerodynamic influence of the various parameters, as well as to gain insight where experiments are limited.

Acknowledgments

This research was supported, in part, by the Nancy and Stephen Grand Technion Energy Program and the Israeli Ministry of Energy.

6 References

[1] Qiu H, You F. Decentralized-distributed robust electric power scheduling for multi-microgrid systems. Appl Energy 2020;269:115146. https://doi.org/10.1016/j.apenergy.2020.115146.

[2] Neto PBL, Saavedra OR, Oliveira DQ. The effect of complementarity between solar, wind and tidal energy in isolated hybrid microgrids. Renew Energy 2020;147:339–55. https://doi.org/10.1016/j.renene.2019.08.134.

[3] Torres-Madroñero JL, Alvarez-Montoya J, Restrepo-Montoya D, Tamayo-Avendaño JM, Nieto-Londoño C, Sierra-Pérez J. Technological and operational aspects that limit small wind turbines performance. Energies 2020;13:6123. https://doi.org/10.3390/en13226123.

[4] Möllerström E, Gipe P, Beurskens J, Ottermo F. A historical review of vertical axis wind turbines rated 100 kW and above. Renew Sustain Energy Rev 2019;105:1–13. https://doi.org/10.1016/j.rser.2018.12.022.

[5] MacPhee D, Beyene A. Recent Advances in Rotor Design of Vertical Axis Wind Turbines. Wind Eng 2013;36:647–65. https://doi.org/10.1260/0309-524x.36.6.647.

[6] Lee KY, Tsao SH, Tzeng CW, Lin HJ. Influence of the vertical wind and wind direction on the power output of a small vertical-axis wind turbine installed on the rooftop of a building. Appl Energy 2018;209:383–91. https://doi.org/10.1016/j.apenergy.2017.08.185.

[7] Keisar D, De Troyer T, Greenblatt D. Concept and operation of a wind turbine driven by dynamic stall. AIAA J 2020;58:2370–6. https://doi.org/10.2514/1.J059487.

[8] Jumper EJ, Schreck SJ, Dimmick RL. Lift-curve characteristics for an airfoil pitching at constant rate. J Aircr 1987;24:680–7. https://doi.org/10.2514/3.45507.

[9] Carr LW. Progress in analysis and prediction of dynamic stall. J Aircr 1988;25:6–17. https://doi.org/10.2514/3.45534.

[10] Qing'an Lia, Maedab T, Kamadab Y, Muratab J, Shimizub K, Ogasawarab T, et al. Effect of solidity on aerodynamic forces around straight-bladedvertical axis wind turbine by wind tunnel experiments (depending on number of blades). Renew Energy 2016:92–939. https://doi.org/.1037//0033-2909.I26.1.78.

[11] Rezaeiha A, Montazeri H, Blocken B. Towards optimal aerodynamic design of vertical axis wind turbines: Impact of solidity and number of blades. Energy 2018;165:1129–48. https://doi.org/10.1016/j.energy.2018.09.192.

[12] Zanforlin S, Deluca S. Effects of the Reynolds number and the tip losses on the optimal aspect ratio of straight-bladed Vertical Axis Wind Turbines. Energy 2018;148:179–95. https://doi.org/10.1016/j.energy.2018.01.132.

[13] Li G, Xu W, Li Y, Wang F. Univariate analysis of scaling effects on the aerodynamics of vertical axis wind turbines based on high-resolution numerical simulations: The Reynolds number effects. J Wind Eng Ind Aerodyn 2022;223. https://doi.org/10.1016/j.jweia.2022.104938.

[14] Keisar D, Eilan B, Greenblatt D. High Pressure Vertical Axis Wind Pump. J Fluids Eng Trans ASME 2021;143:1–9. https://doi.org/10.1115/1.4049692.

[15] Thelander CG, Smallwood KS, Rugge L. Bird Risk Behaviors and Fatalities at the Altamont Pass Wind Resource Area. Subcontract Rep NREL/SR-500-33829 2003:92 pp.

[16] Ghasemian M, Nejat A. Aero-acoustics prediction of a vertical axis wind turbine using Large Eddy Simulation and acoustic analogy. Energy 2015;88:711–7. https://doi.org/10.1016/j.energy.2015.05.098.

[17] Lentink D, Dickinson MH. Rotational accelerations stabilize leading edge vortices on revolving fly wings. J Exp Biol 2009;212:2705–19. https://doi.org/10.1242/jeb.022269.

[18] Paraschivoiu I. Double-multiple streamtube model for studying vertical-axis wind turbines. J Propuls Power 1988;4:370–7. https://doi.org/10.2514/3.23076.

[19] Mueller-Vahl H, Strangfeld C, Nayeri CN, Paschereit CO, Greenblatt D. Thick Airfoil Deep Dynamic Stall. In: M. Hölling JP and SI, editor. Wind Energy – Impact ofTurbulence, Springer-Verlag Berlin Heidelberg; 2014, p. 35–40. https://doi.org/10.1007/978-3-642-54696-9_6.

[20] Medina A, Ol M V., Greenblatt D, Müller-Vahl H, Strangfeld C. High-Amplitude Surge of a Pitching Airfoil: Complementary Wind- and Water-Tunnel Measurements. AIAA J 2018;56:1703–9. https://doi.org/10.2514/1.j056408.

[21] Müller-Vahl HF, Pechlivanoglou G, Nayeri CN, Paschereit CO, Greenblatt D. Matched pitch rate extensions to dynamic stall on rotor blades. Renew Energy 2017;105:505–19. https://doi.org/10.1016/j.renene.2016.12.070.

[22] Müller-Vahl HF, Strangfeld C, Nayeri CN, Paschereit CO, Greenblatt D. Dynamic Stall Under Combined Pitching and Surging. AIAA J 2020;58:5134–45. https://doi.org/10.2514/1.J059153.

[23] Corke TC, Thomas FO. Dynamic Stall in Pitching Airfoils : Aerodynamic Damping and Compressibility Effects 2015. https://doi.org/10.1146/annurev-fluid-010814-013632.

[24] Migliore PG, Wolfe WP, Fanucci JB. Flow Curvature Effects on Darrieus Turbine Blade Aerodynamics. J Energy 1980;4:49–55. https://doi.org/10.2514/3.62459.

[25] Fiedler AJ, Tullis S. Blade offset and pitch effects on a high solidity vertical axis wind turbine. Wind Eng 2009;33:237–46. https://doi.org/10.1260/030952409789140955.

[26] Nguyen MT, Balduzzi F, Goude A. Effect of pitch angle on power and hydrodynamics of a vertical axis turbine. Ocean Eng 2021;238:109335. https://doi.org/10.1016/j.oceaneng.2021.109335.

[27] Daley DG, Jumpert EJ. Experimental investigation of dynamic stall for a pitching airfoil. J Aircr 1984;21:831–2. https://doi.org/10.2514/3.45050.

[28] Lee T, Gerontakos P. Investigation of flow over an oscillating airfoil. J Fluid Mech 2004;512:313–41. https://doi.org/10.1017/S0022112004009851.

[29] Choudhry A, Leknys R, Arjomandi M, Kelso R. An insight into the dynamic stall lift characteristics. Exp Therm Fluid Sci 2014;58:188–208. https://doi.org/10.1016/j.expthermflusci.2014.07.006.

[30] Greenblatt D, Neuburger D, Wygnanski I. Dynamic stall control by intermittent periodic excitation. J Aircr 2001;38:188–9. https://doi.org/10.2514/2.2751.

[31] Müller-Vahl HF, Strangfeld C, Nayeri CN, Paschereit CO, Greenblatt D. Control of thick airfoil, deep dynamic stall using steady blowing. AIAA J 2015;53:277–95. https://doi.org/10.2514/1.J053090.

[32] Strickland JH, Graham GM. Force coefficients for a NACA-0015 airfoil undergoing constant pitchrate motions. AIAA J 1987;25:622–4. https://doi.org/10.2514/3.9673.

[33] Visbal MR. Dynamic stall of a constant-rate pitching airfoil. J Aircr 1990;27:400–7. https://doi.org/10.2514/3.25289.

[34] Le Fouest S, Mulleners K. The dynamic stall dilemma for vertical-axis wind turbines. Renew Energy 2022;198:505–20. https://doi.org/10.1016/j.renene.2022.07.071.

[35] Yang Y, Guo Z, Zhang Y, Jinyama H, Li Q. Numerical investigation of the tip vortex of a straight-bladed vertical axis wind turbine with double-blades. Energies 2017;10:1721. https://doi.org/10.3390/en10111721.

[36] Greenblatt D. Unsteady Low-Speed Wind Tunnels. AIAA J 2016;54:1817–30. https://doi.org/10.2514/1.J054590.

[37] Kinsey T, Dumas G. Impact of channel blockage on the performance of axial and cross-flow hydrokinetic turbines. Renew Energy 2017;103:239–54. https://doi.org/10.1016/j.renene.2016.11.021.

[38] Brusca S, Lanzafame R, Messina M. Design of a vertical-axis wind turbine: how the

aspect ratio affects the turbine's performance. Int J Energy Environ Eng 2014;5:333–40. https://doi.org/10.1007/s40095-014-0129-x.

[39] Miller MA, Duvvuri S, Brownstein I, Lee M, Dabiri JO, Hultmark M. Vertical-axis wind turbine experiments at full dynamic similarity. J Fluid Mech 2018;844:707–20. https://doi.org/10.1017/jfm.2018.197.

[40] Greenblatt D, Wygnanski I. Effect of leading-edge curvature on separation control - A comparison of two NACA airfoils. 40th AIAA Aerosp. Sci. Meet. Exhib., American Institute of Aeronautics and Astronautics; 2002. https://doi.org/doi:10.2514/6.2002-411.

[41] Greenblatt D. Active control of leading-edge dynamic stall. Int J Flow Control 2010;2:21–38. https://doi.org/10.1260/1756-8250.2.1.21.

[42] Jain S, Saha UK. On the influence of blade thickness-to-chord ratio on dynamic stall phenomenon in H-type Darrieus wind rotors. Energy Convers Manag 2020;218. https://doi.org/10.1016/j.enconman.2020.113024.

[43] Wang P, Wang L, Kong X, Wu D, Huang B. Influence of relative thickness on static and dynamic stall characteristics and prediction of airfoils. Ocean Eng 2023;271. https://doi.org/10.1016/j.oceaneng.2023.113690.

[44] Sheldahl RE, Klimas PC. Aerodynamic characteristics of seven symmetrical airfoil sections through 180-degree angle of attack for use in aerodynamic analysis of vertical axis wind turbines (SAND-80-2114). Albuquerque, NM (United States): 1981. https://doi.org/10.2172/6548367.

[45] Abbott IH, Von Doenhoff AE. Theory of wing sections. vol. 249. New York: 1950. https://doi.org/10.1016/0016-0032(50)90516-3.

[46] Somoano M, Huera-Huarte FJ. The dead band in the performance of cross-flow turbines: Effects of Reynolds number and blade pitch. Energy Convers Manag 2018;172:277–84. https://doi.org/10.1016/j.enconman.2018.06.087.

[47] Armstrong S, Fiedler A, Tullis S. Flow separation on a high Reynolds number, high solidity vertical axis wind turbine with straight and canted blades and canted blades with fences. Renew Energy 2012;41:13–22. https://doi.org/10.1016/j.renene.2011.09.002.

[48] Miller MA, Duvvuri S, Kelly WD, Hultmark M. Rotor solidity effects on the performance of vertical-axis wind turbines at high Reynolds numbers. J Phys Conf Ser 2018;1037. https://doi.org/10.1088/1742-6596/1037/5/052015.

[49] Miller MA, Duvvuri S, Hultmark M. Solidity effects on the performance of vertical-axis wind turbines. Flow 2021;1:1–15. https://doi.org/10.1017/flo.2021.9.

[50] Peng HY, Zhong BW, Hu G, Liu HJ. Optimization analysis of straight-bladed vertical

axis wind turbines in turbulent environments by wind tunnel testing. Energy Convers Manag 2022;257. https://doi.org/10.1016/j.enconman.2022.115411.

[51] Miller MA, Kiefer J, Westergaard C, Hansen MOL, Hultmark M. Horizontal axis wind turbine testing at high Reynolds numbers. Phys Rev Fluids 2019;4:1–22. https://doi.org/10.1103/PhysRevFluids.4.110504.

[52] Ross I, Altman A. Wind tunnel blockage corrections: Review and application to Savonius vertical-axis wind turbines. J Wind Eng Ind Aerodyn 2011;99:523–38. https://doi.org/10.1016/j.jweia.2011.02.002.

[53] Lorber PF, Carta FO. Airfoil dynamic stall at constant pitch rate and high Reynolds number. J Aircr 1988;25:548–56. https://doi.org/10.2514/3.45621.

[54] Francis MS, Keesee JE. Airfoil dynamic stall performance with large-amplitude motions. AIAA J 1985;23:1653–9. https://doi.org/10.2514/3.9146.

[55] Buchner A-J, Soria J, Honnery D, Smits AJ. Dynamic stall in vertical axis wind turbines: scaling and topological considerations. J Fluid Mech 2018;841:746–66. https://doi.org/10.1017/jfm.2018.112.

[56] Rezaeiha A, Kalkman I, Blocken B. Effect of pitch angle on power performance and aerodynamics of a vertical axis wind turbine. Appl Energy 2017;197:132–50. https://doi.org/10.1016/j.apenergy.2017.03.128.

[57] Zhang LX, Liang Y Bin, Liu XH, Guo J. Effect of blade pitch angle on aerodynamic performance of straight-bladed vertical axis wind turbine. J Cent South Univ 2014;21:1417–27. https://doi.org/10.1007/s11771-014-2080-7.

[58] Yang Y, Guo Z, Song Q, Zhang Y, Li Q. Effect of blade pitch angle on the aerodynamic characteristics of a straight-bladed vertical axis wind turbine based on experiments and simulations. Energies 2018;11:1514. https://doi.org/10.3390/en11061514.

[59] Guo Y, Li X, Sun L, Gao Y, Gao Z, Chen L. Aerodynamic analysis of a step adjustment method for blade pitch of a VAWT. J Wind Eng Ind Aerodyn 2019;188:90–101. https://doi.org/10.1016/j.jweia.2019.02.023.

[60] Jumper EJ, Dimmick RL, Allaire AJS. The effect of pitch location on dynamic stall. J Fluids Eng Trans ASME 1989;111:256–62. https://doi.org/10.1115/1.3243639.

[61] Kumar V, Paraschivoiu M, Paraschivoiu I. Low reynolds number vertical axis wind turbine for mars. Wind Eng 2010;34:461–76. https://doi.org/10.1260/0309-524X.3.4.461.

[62] Migliore PG. Comparison of NACA 6-series and 4-digit airfoils for Darrieus wind turbines. J Energy 1983;7:291–2. https://doi.org/10.2514/3.48083.

[63] Keisar D, Freger V, Greenblatt D. Direct wind-powered vertical axis brackish water desalination system. Desalination 2024;570:117060. https://doi.org/https://doi.org/10.1016/j.desal.2023.117060.

[64] Grieser B, Sunak Y, Madlener R. Economics of small wind turbines in urban settings: An empirical investigation for Germany. Renew Energy 2015;78:334–50. https://doi.org/https://doi.org/10.1016/j.renene.2015.01.008.

[65] Peri E, Becker N, Tal A. What really undermines public acceptance of wind turbines? A choice experiment analysis in Israel. Land Use Policy 2020;99:105113. https://doi.org/https://doi.org/10.1016/j.landusepol.2020.105113.

[66] Teschner N, Alterman R. Preparing the ground: Regulatory challenges in siting small-scale wind turbines in urban areas. Renew Sustain Energy Rev 2018;81:1660–8. https://doi.org/10.1016/j.rser.2017.05.256.